Conference on Energy Sustainability
ES2021
June 16-18, 2021, Virtual, Online

ES2021-63938

EFFECT OF PHASE CHANGE AND BUOYANCY-DRIVEN FLOWS ON AN ROC-BASED THERMAL ENERGY STORAGE SYSTEM

Justin Andrew Lee, Christopher N. Salerno, Karen U. Girgis, Ulyses Aguirre, and Reza Baghaei Lakeh*

Mechanical Engineering Department
California State Polytechnic University, Pomona,
Pomona, California, USA

ABSTRACT

Inorganic salts (e.g., chloride salts) have gained attention in the energy field as a new thermal energy storage medium. Low cost, high melting temperature and high heat capacity of inorganic salts make them attractive in utility-scale thermal storage applications as higher energy storage temperatures lead to higher efficiency in power generation. There is a potential to use the dry byproduct of water desalination, i.e., Reverse Osmosis Concentrate (ROC) as a thermal storage medium. Using ROC as a thermal energy storage medium would prevent a harmful waste to be released to the environment while introducing a novel and low-cost alternative for thermal energy storage medium. In this study, heat transfer behavior of an ROC-based thermal energy storage system is studied using CFD. A computational model is developed, verified, and validated to simulate the phase change process and buoyancy-driven flow in a square ROC-based thermal energy storage element. The computational results provide a predictive model for charge and discharge cycles of an ROC-based thermal energy storage system.

Keywords: computational fluid dynamics (FLUENT), phase change material, reverse osmosis concentrate

NOMENCLATURE

A_s	Surface Area (m^2)
A_{mush}	Mushy Zone Constant ($kg/sec*m^3$)
c_p	Specific Heat (J/kg-K)
g	Gravity (m/s^2)
E	Energy, (J)
H	Enthalpy, (J)
h	Sensible Enthalpy (J)
h_c	Convective Heat Transfer Coefficient (W/m^2-K)
k	Thermal Conductivity, (W/m-K)
T	Temperature, (°C)
T_{cold}	constant cold temperature, (°C)
T_{hot}	constant hot temperature, (°C)
T_S	Solidus Temperature, (°C)
T_L	Liquidus Temperature, (°C)
T_∞	Bulk Fluid Temperature (°C)
T*	Dimensionless temperature
V_c	Control Volume (m^3)

Greek Symbols

β	Thermal Expansion Coefficient (K^{-1})
ε	Small number, 0.001, to prevent division by 0
μ	Viscosity (kg/m-sec)
υ	Velocity (m/sec)
ρ	Density (kg/m^3)

1. INTRODUCTION

Due to the increase of global warming in the last decade, governments have been focused on utilizing renewable energy sources, such as solar, wind, and hydro to provide the necessary energy for the power grid. Solar energy, in particular, has many advantages such as being a clean, affordable, and widely distributable alternative compared with other renewable energy sources. However, the widespread application of solar energy is limited by its intermittent availability caused by changes in cloud coverage and angle of incident varied by the season. Thermal Energy Storage (TES) is one of the methods of storing excess solar thermal power and then delivering that power back to the grid when demand outpaces availability of solar energy. Phase Change Materials (PCM) are particularly of interest as TES mediums due to their higher energy storage density.

*Corresponding Author: rblakeh@cpp.edu

Inorganic salts as a low-cost TES medium are well-suited to address the higher operating temperature needs of solar power towers. Inorganic salts can be used as heat transfer fluids (HTFs) and/or TES media in advanced high-temperature concentrating solar power plants (CSP) [1]. The use of ROC as a high temperature TES medium allows for higher efficiency of steam power generation, in comparison to the use of nitrate-based salts (NaNO3/KNO3). Typical Solar Salt with a 60/40 weight ratio of NaNO3 and KNO3 melts at 220 °C and is stored hot at 565 °C [2] whereas the ROC goes through liquid-solid phase change between 550 °C to 638 °C depending on the feedwater source. Using ROC salt as a TES has the potential to prevent environmental harm caused by the discharge of ROC to the environment [3]. The TESuROC (Thermal Energy Storage using Reverse Osmosis Concentrate) Project is motivated to find an alternative thermal energy storage solution that both improves the efficiency of current TES systems and decreases the environmental impact of water desalination.

The TESuROC project aims to study how to repurpose ROC in traditional TES systems that can be charged by direct solar thermal or electric resistive heating. In order to predict the heat transfer and visualize the natural convection activity during the charging period Computational Fluid Dynamics (CFD) was employed. The main objective of this study is to study the heat transfer characteristics of an ROC-based TES system. The results show that heat transfer during charge cycle is highly impacted by solid-liquid phase change, buoyancy-driven flow and Rayleigh-Bernard instability.

1.1 TESuROC Prototype

The team fabricated a prototype of the TES device that contains an ROC mixture in its salt tube as shown in Figure. 1. The chamber and baffles surrounding this salt element is run with hot air is generated by a *Heat Torch ™ 200*, a Tutco-Farnam custom heater, which outputs a maximum air temperature of roughly 700 °C. The results of the experimental study are presented in a separate paper.

2. COMPUTATIONAL MODEL AND MATHEMATICAL FORMULATION

A computational model was developed in ANSYS Fluent version 2020 R1 to analyze the heat transfer behavior of the ROC salt during the charging phase. The model simulates the phase change and buoyancy-driven flow within a simplified 2D computational domain representing a cross section of the square tube as shown in Figure 2.

2.1 Geometry

The length of the salt tube is more than one order of magnitude larger that the hydrodynamic diameter of the tube; therefore, the end effects are neglected and a 2D computational domain is adopted. The turbulent mixing of the air by the baffles provides a nearly uniform wall temperature around the cross section of the tube. This simplifies the boundary condition of the walls to that of a constant temperature.

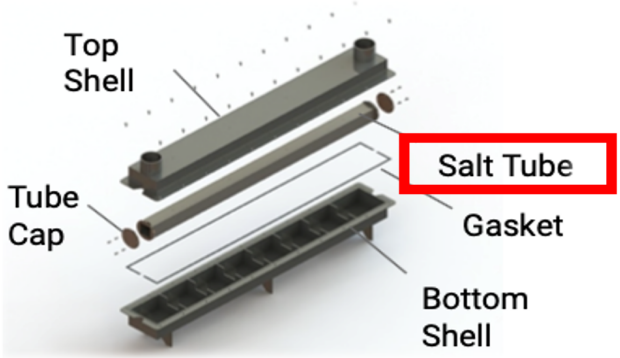

FIGURE 1. Breakdown of the TES prototype device. Emphasizing the salt tube.

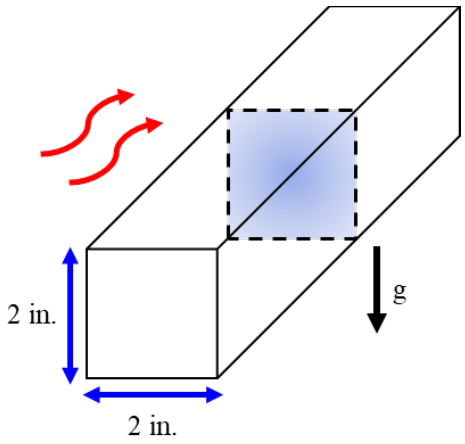

FIGURE 2. The cross section of the salt tube for 2D computation.

2.2 ROC Composition and Melting Temperature

The ROC is composed primarily of the salts that naturally occur in bodies of water with different ions such as sodium, potassium, calcium magnesium, chlorides, carbonates, and bicarbonates as illustrated in Figure 3 different bodies of water are expected to be composed of varying levels of these ions, so as an early assessment of the ROC's composition, the dry composition of sea water is used. The thermophysical properties of the ROC are held constant, except for density.

Experimental salt degradation testing gives an average melting temperature of 609 °C with the earliest observation of melting at 560 °C and latest at 647 °C as shown in Figure 4 as the salt mixture is expected to have a range for melting temperature, the simulated melting was estimated to occur at a range of one standard deviation of the average recorded temperature at which melting was observed. This gives the solidus temperature of 579.85 °C and liquidus temperature of 638.48 °C.

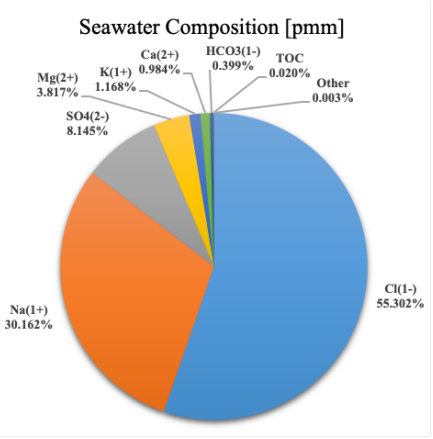

FIGURE 3. example of ROC chemical composition using seawater as feed.

Thermophysical composition of ROC such as specific heat, thermal conductivity, and viscosity were held constant with a reference temperature of 814°C as tabulated in Table 1 sea water chemical composition shows that chemical composition of the ROC salt is dominated by sodium and chlorine ions that make up sodium chloride salt. Since the assumed primary component to ROC is sodium chloride salt, its properties were chosen for the constant thermophysical properties in order to model melting. The properties of the ROC are expected to vary depending on the feedwater source of the desalination plants, these properties are assumed constant to provide a preliminary understanding of the melting behavior of ROC salt in elevated temperatures.

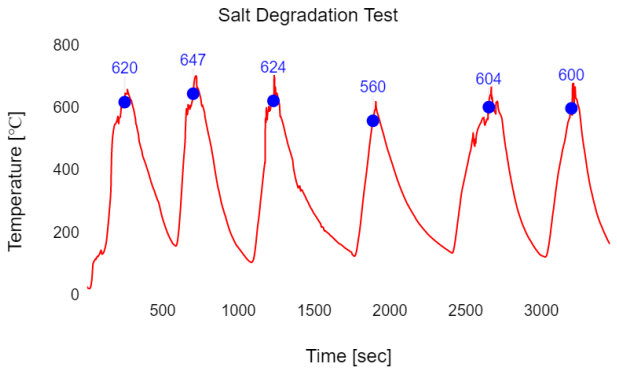

FIGURE 4. Temperature cycling of the ROC where blue dots indicate when melting was visually observed.

TABLE 1. Properties of ROC with much of its thermophysical properties of that of sodium chloride.

ROC Properties, T_{ref} = 814°C	
Solidus Temperature, $T_{solidus}$, (°C)	579.85
Liquidus Temperature, $T_{liquidus}$, (°C)	638.48
Density, ρ, (kg/m^3)	1514
Specific Heat, c_p, (J/kg-K)	1058.35
Viscosity, μ, (kg/m-sec)	0.00103
Thermal Conductivity, k, (W/m-K)	0.497
Thermal Expansion Coefficient, β, (K^{-1})	0.000345
Pure Solvent Melting Heat, L_m, (J/kg)	520000

2.3 Governing Equations

To simulate the charging phase, ANSYS Fluent solves the mass, momentum, and energy conservation equations given by Eqs. (1-3) [5].

$$\frac{\partial}{\partial t}(\rho) + \nabla \cdot (\rho \vec{v}) = 0 \quad (1)$$

$$\frac{\partial}{\partial t}(\rho \vec{v}) + \nabla \cdot (\rho \vec{v} \vec{v}) = -\nabla p + \nabla \cdot (\bar{\bar{\tau}}) + p\vec{g} + \vec{F} \quad (2)$$

$$\frac{\partial}{\partial t}(\rho E) + \nabla \cdot [\vec{v}(\rho E + p)] = \nabla \cdot \left[k \nabla T - \sum_j h_j \vec{J_j} + (\bar{\bar{\tau}} \cdot \vec{v}) \right] \quad (3)$$

2.4 Natural Convection

The Boussinesq approximation was used to model natural convection by assuming density as a constant value for all equations except for the buoyancy term , $\rho\vec{g}$, in the momentum equation in which density varies linearly with temperature

according to Eq. 4. The presence of gravity affects the buoyancy term and is responsible for the effects of natural convection where the buoyant molten ROC salt rises and displaces denser fluid. The buoyancy driven flow enhances heat transfer by increasing flow activity near the solid-liquid interface and all solid walls.

$$\rho \approx \rho_{\circ}\big(1 - \beta(T - T_{\circ})\big) \tag{4}$$

2.5 Solidification and Melting

For pure substances melting in isobaric conditions, the phase change process occurs at a narrow temperature range. However, most salt hydrates show phase change over a larger temperature range instead of a single temperature [6]. It has been shown that phase change materials reach complete melting over a temperature range sooner compared to a constant temperature [7]. This leads to significant errors between experimental and numerical results; thus, the melting model should take into account a temperature range which is defined by the solidus and liquidus temperatures for the ROC.

Enthalpy-porosity technique is used to simulate melting, where the melting interface is tracked implicitly using the liquid fraction of each cell [8-10]. The liquid fraction is the normalized proportion of liquid phase in each cell volume computed at each iteration based on the enthalpy balance. The cells that yield a liquid fraction between 0 to 1 define the "mushy zone" which is modeled as a porous medium [5]. The enthalpy takes into account the sensible enthalpy and latent heat given by Eqs. (5-6) [5].

$$H = h + \Delta H \tag{5}$$

Where

$$H = h_{ref} + \int_{T_{ref}}^{T} c_p dT \tag{6}$$

The liquid fraction is calculated using Eq.7. [5]

$$\beta = \begin{cases} 0 & if \quad T_S > T \\ \dfrac{T - T_S}{T_L - T_S} & if \quad T_S < T < T_L \\ 1 & if \quad T > T_L \end{cases} \tag{7}$$

Now, the latent heat can be rewritten in terms of the latent heat of the material that ranges from zero for a solid and L for a liquid given by Eq.8. [5]

$$\Delta H = \beta L \tag{8}$$

The energy conservation equation for solidification and melting is given by Eq.9 [5].

$$\frac{\partial}{\partial t}(\rho H) + \nabla \cdot [\vec{v}(\rho H)] = \nabla \cdot [k \nabla T] + S \tag{9}$$

The temperature for each cell is found iterating between Eq. (7) and Eq.9, where liquid fraction is updated by Voller and Swaminathan method to improve convergence [10]. In the mushy zone, an additional source term is introduced in Eq. (2) which accounts for the loss in momentum as the porosity is reduced given by Eq.10 [5].

$$S = \frac{(1 - \beta)^2}{(\beta^2 + \varepsilon)} A_{mush}\big(\vec{v} - \vec{v}_p\big) \tag{10}$$

When examining the temperature of the charge and discharge cycles with different hot and cold temperature boundary conditions, it is useful to represent the temperature in dimensionless form. Eq (11) is how dimensionless temperature is calculated, where in the charge cycle the T_{hot} would be the constant wall temperature and the T_{cold} was the initial temperature, and in the discharge cycle the T_{hot} was the initial temperature and the T_{cold} is the constant wall temperature.

$$T^* = \frac{T - T_{Cold}}{T_{Hot} - T_{Cold}} \tag{11}$$

2.6 Transient Heat Transfer Approximation

Thermal energy storage is inherently a transient problem and to determine the amount of time necessary to bring the thermal storage medium to a desired temperature requires a transient heat transfer model. The lumped capacitance model is a simplified transient heat transfer model that can be used to estimate the temperature inside the thermal energy storage device. This model will serve as validation for the temperature change during simulation.

$$\frac{\theta}{\theta_i} = \frac{T - T_{\infty}}{T_i - T_{\infty}} = exp\left[-\left(\frac{h_c A_s}{\rho V_c}\right) t\right] \tag{12}$$

2.7 Computational Model

The transient CFD model was solved using a pressure-based type solver and applying gravitational acceleration. The energy equation model was activated to account for the heat transfer along with the Solidification and Melting model for the phase change. The calculated Rayleigh number for the charging

process is $1.98x10^{+8}$, where the length scale is the side length of 2 inches. This Rayleigh number with a magnitude of 10^{+8} indicates that the flow is laminar, so the laminar viscous model was used which does not introduce any additional flow equations to be solved. The Boussinesq approximation was applied to the material density property using the reference temperature of 814°C as the operating temperature in Eq (4). A pressure-based coupled algorithm was used to couple the momentum and pressure-based continuity equation which improved the rate of solution convergence. The default least-squares cell based gradient method was chosen to reduce computational expense compared to the node-based gradient. Pressure was solved using the second order interpolation scheme. The momentum and energy equations were discretized using second order windup schemes. The convergence criteria were specified that the continuity and momentum equation residuals be reduced below 10^{-3} for each timestep, while the energy residuals be reduced below 10^{-6} at each timestep.

2.8 Boundary and Initial Conditions

Table 2 summarizes initial and boundary conditions of the computations. The simple geometry of the computational domain was fitted with a simple mesh composed of quadrilateral grids with clusters around the walls to resolve high velocity and temperature gradients. Charge cycle occurs from an initial temperature of 290°C to 700°C, which is the maximum temperature of the *Heat Torch ™ 200* installed on the prototype TES device. Discharge cycle occurs at the fully charged state and its energy is extracted from a heat transfer fluid that enters the TES device at 290°C [15] Organic Rankine cycle operation, forming the 290°C wall temperature boundary. In this round of simulation, a look at the cross section of the leading end of the salt element is simulated for melting behavior. It is expected that there will be a gradient of bulk mean temperature along the axial direction of the tube, however this snapshot at the leading end will inform how natural convection affects the total heat transfer capabilities at the hottest end of the TES device.

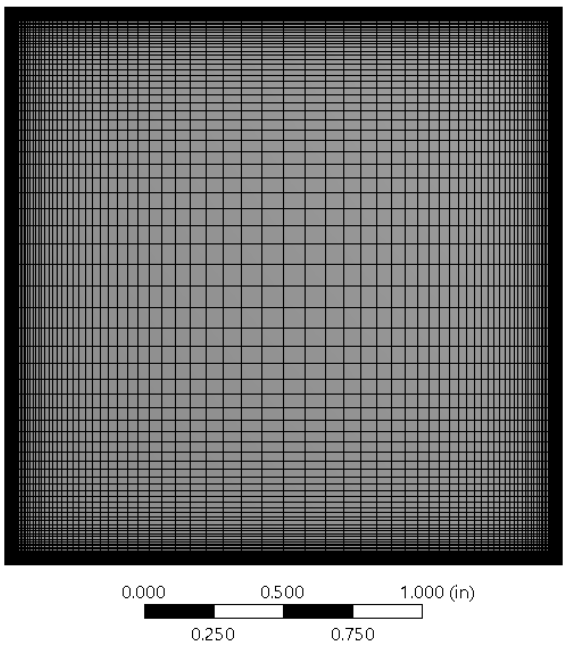

FIGURE 5. Mesh of cross section showing quadrilateral grids with bias towards edges. This is 100x100. Boundary and initial conditions also labeled.

TABLE 2. Boundary conditions for charge and discharge

Boundary Conditions	Charge	Discharge
Wall Temperature [°C]	700	290
Initial Temperature [°C]	290	700
Initial Velocity [m/sec]	0	0
Shear Condition	No slip	

2.9 Verification and Validation

A grid refinement study was performed to confirm that the results are independent of the computational grid. Three different grids with significantly different number of computational grids were used. The first trial was a 100x100 grid while the second and third grids are 175x175, and 300x300 respectively. The results are the grid refinement study is presented in Figure 6. An asymptotic behavior is observed in the results when the number of the grid points is 3X and 9X more than the original mesh, confirming that the results are grid independent. Confirming grid independency, the 300x300 grid was used to generate the plots and data for the discussion.

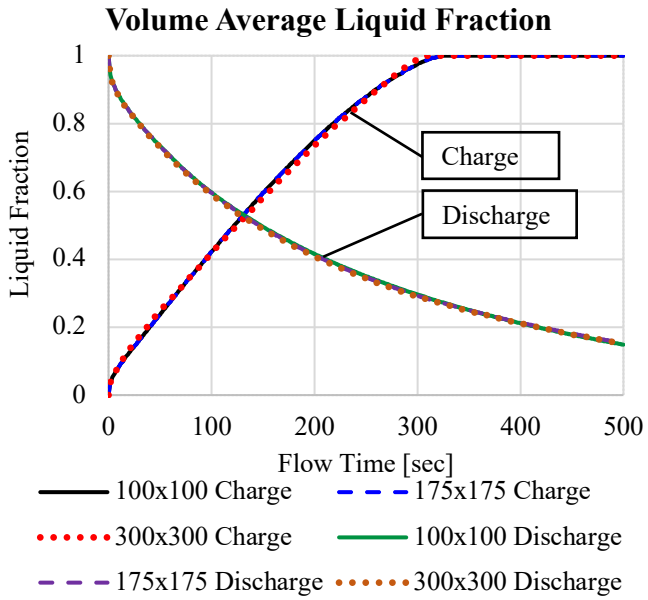

FIGURE 6. Liquid fraction charge and discharge for all grids.

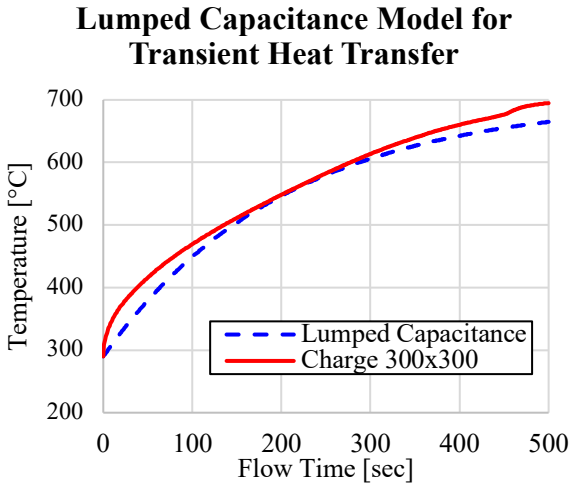

FIGURE 7. Lumped capacitance model for the transient heat transfer rate for the charge cycle.

Using the lumped capacitance model to calculate the average temperature and superimposing it over the simulated average temperature, seen in Figure 7, reveals the usefulness of this approximation. Though this model has a maximum relative error of 13%, since the ROC material is expected to vary from difference sources this error can guide the design of a thermal energy storage device by broadening its operation range for a variety of ROC compositions.

3. RESULTS AND DISCUSSION

Figure 8 shows the history of the temperature field in the ROC salt during charge cycle. These temperatures are represented by their dimensionless temperatures to better compare the temperature distribution with different temperature boundary and initial conditions. The left side showing charging phase, Figure 8a, shows fluid flow during melting, which speeds up the melting process. The right side showing discharging phase, Figure 8b, shows a buildup of cold and solidified material along the walls effectively insulating the remaining molten salt.

As expected, the flow and temperature fields are highly impacted by buoyancy-driven flow and phase change process. Figure 9-14 show the contour plots of liquid fraction, flow streamlines and temperature at 150 s after the start of charging. Distinct liquid and solid states of the ROC salt is clearly observed, and the interface is tracked by the mushy zone. The result show that the natural convection is manifested in the liquid phase by boundary layer formation on the vertical walls of the tube and Rayleigh-Bernard instability on the horizontal bottom wall of the tube as shown in Figure 9. Comparing contour plots of temperature (Figure 13) with buoyancy-driven streamlines (Figure 11) shows that the melting front (mushy zone) is impacted by the presence of natural convection boundary layer and instability.

The discharge phase does not benefit from the buoyancy driven flow, as the material solidifies from the walls and thickens towards the center, which decreases the length scale for natural convection. Comparing the velocity magnitudes at the same flow time of 150 sec of Figure 15 and Figure **16** show that the discharge phase has an order of magnitude decrease in maximum velocity. The insulating behavior in the discharge cycle has noticeable effect on the average temperature seen in the temperature duration chart on Figure 17.

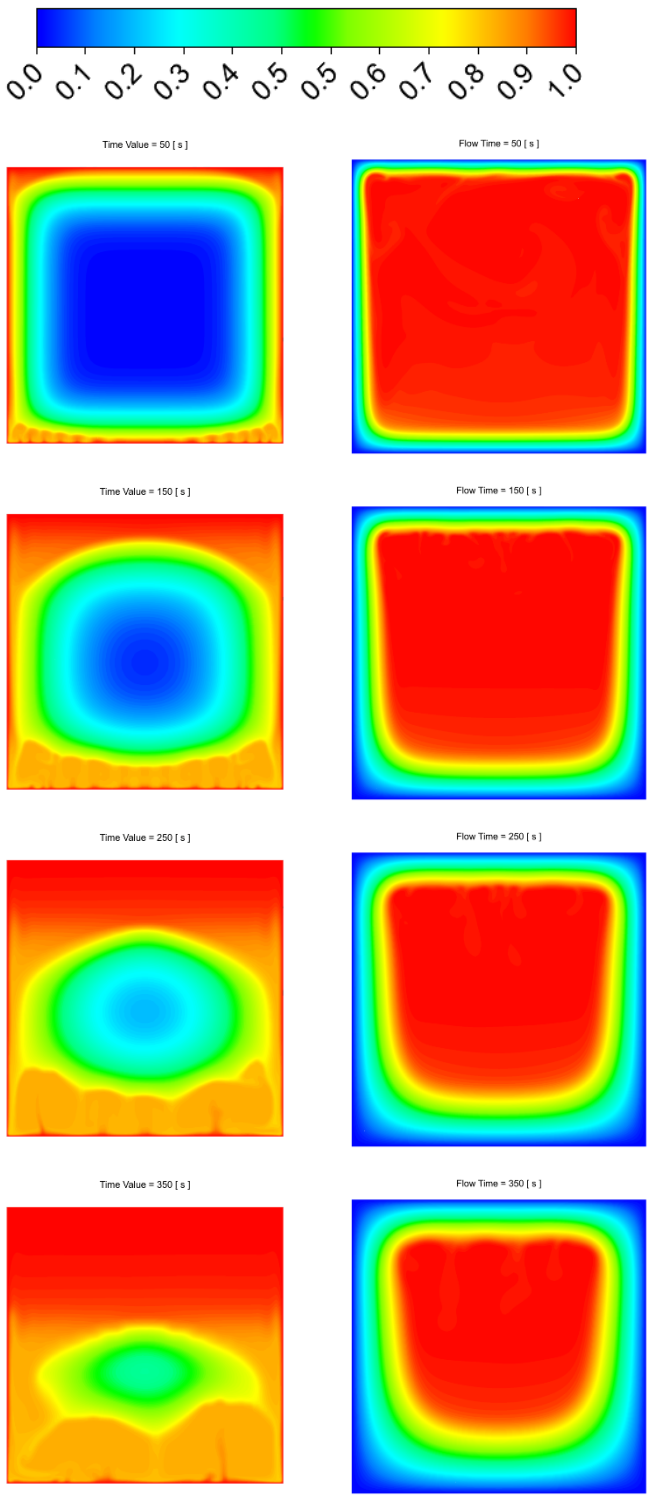

(a) (b)

FIGURE 8. Time-lapse of charge (a) and discharge (b) showing contour plots of dimensionless temperature according to equation 11 on T* from 50,150,250,and 350 sec.

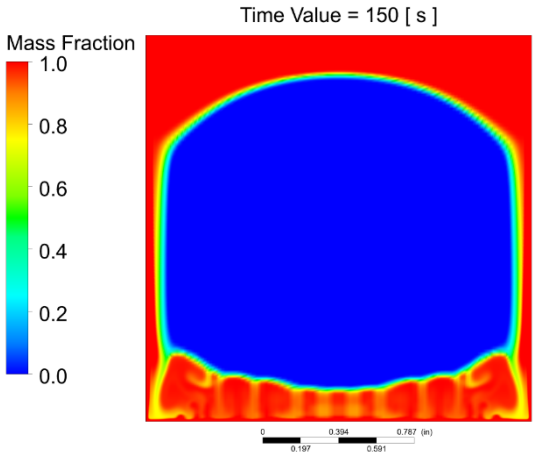

FIGURE 9. Contour plot of charge phase mass/liquid fraction at 150 seconds.

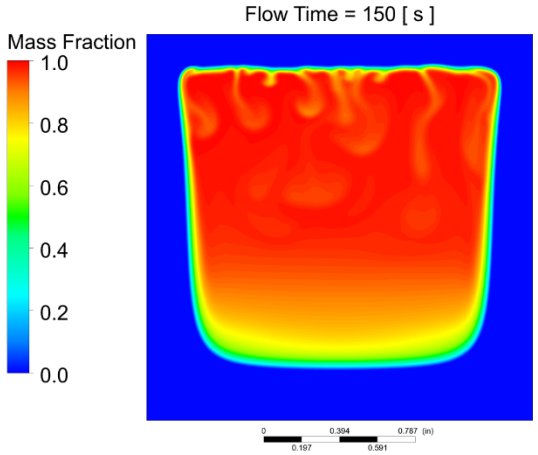

FIGURE 10. Contour plot of discharge phase mass/liquid fraction at 150 seconds.

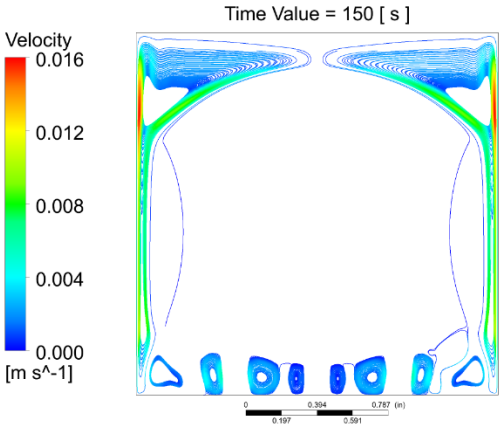

FIGURE 11. Streamline plot of charge phase at 150 seconds where colors represent charge phase velocity magnitude.

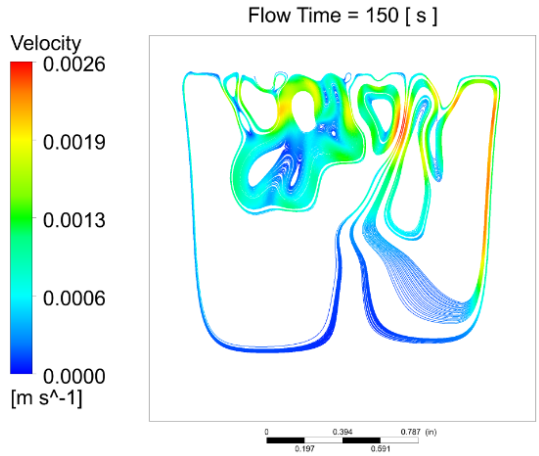

FIGURE 12. Streamline plot of discharge phase at 150 seconds where colors represent charge phase velocity magnitude.

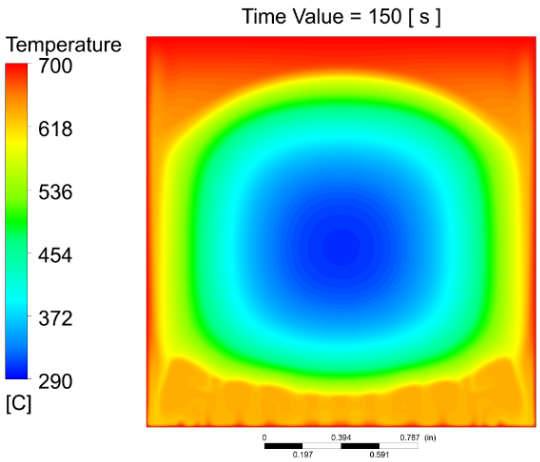

FIGURE 13. Contour plot of charge temperature at 150 seconds.

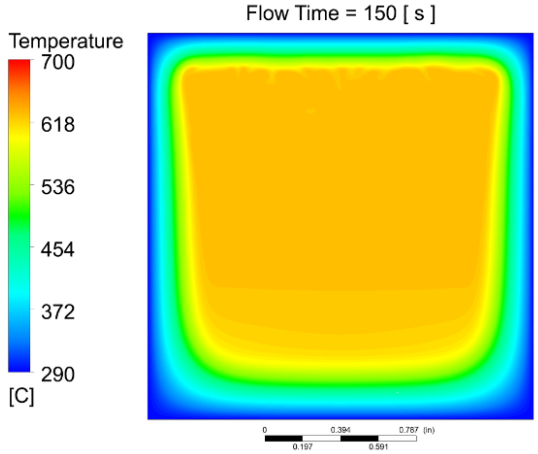

FIGURE 14. Contour plot of discharge temperature at 150 seconds.

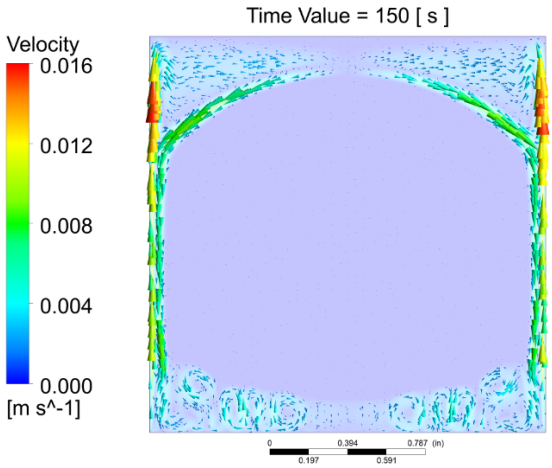

FIGURE 15. Vector plot of charge phase velocity laid over contour plot of velocity magnitude at 150 seconds.

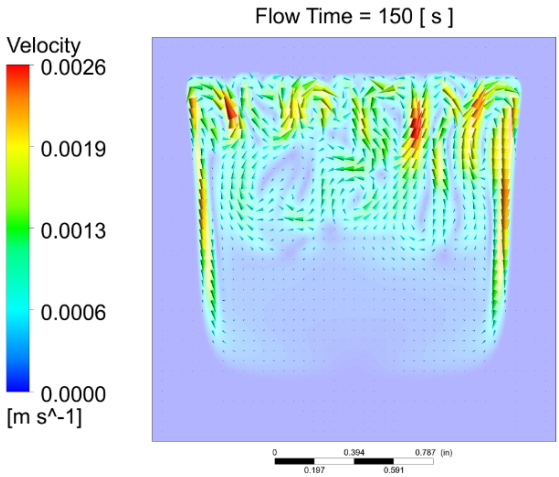

FIGURE 16. Vector plot of discharge phase velocity laid over contour plot of velocity magnitude at 150 seconds.

It is observed that an elongated bell-shaped solid mass to develop inside the square tube during the melting cycle due to presence of natural convection boundary layer on the side walls and Rayleigh-Bernard instability on the bottom wall. The heat transfer initially starts by conduction from all walls to the solid salt. Once the liquidous temperature of the ROC salt is achieved, the ROC salt melts and provides the opportunity for enhanced heat transfer by natural convection. The molten ROC salt near all walls is buoyant and at a higher temperature compared to the mushy zone; therefore, it rises along the side walls and creates a natural convection boundary layer as shown in Figure 13.

A combined velocity magnitude and velocity vector plot was created in Figure 15 to show the direction and magnitude of the flow. This combined plot explains the bell shape solid region in more details throughout its melting process, where the velocity magnitude is greatest along the side walls and is where the most melting occurred. The fluid at the top is warmer so much of the top and the corners are melted away first with much of the melting occurring because of some flow going down the top corner and down the sides. There is more circulation happening at the bottom because the heated fluid rises and meets the solid ROC which is at a lower temperature, thus the liquid transfers its heat and increases the temperature of the solid, then cools and goes back down to be heated by the bottom wall.

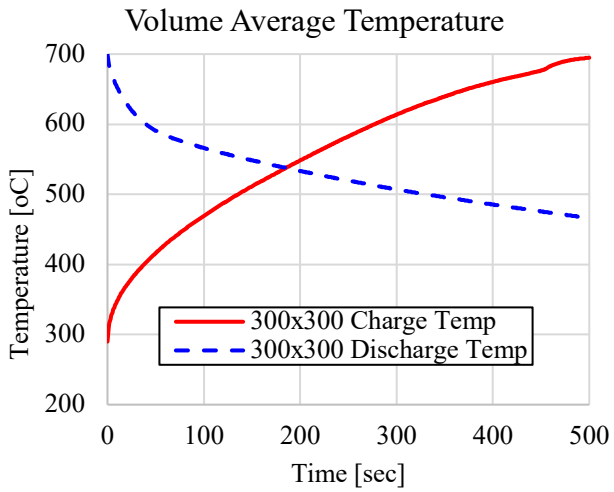

FIGURE 17. Volume average of temperature of the ROC salt.

Figure 6 and Figure 17 that show the volume average of ROC temperature and liquid fraction. A nonlinear increase of temperature with time is observed when melting is taking place. This nonlinear change of temperature is consistent with minor variations of heat flux during phase change process as shown in Figure 18. Once all of the ROC salt is in liquid phase (after about 300 s), the temperature starts increasing at a higher rate due to more flow activity in the absence of solid ROC. Once the average temperature of the ROC salt approaches the wall temperature, heat flux drops to very small values.

There is an inflection with the increase of temperature immediately after the entire solution domain becomes liquid. This inflection occurs at around 450 seconds at which point the temperature increases rapidly for a brief moment before reaching an asymptote with the max temperature of 700°C. This behavior is also seen in other PCMs simulations and experiments such as in Bellan [11-13] and Fornarelli [14].

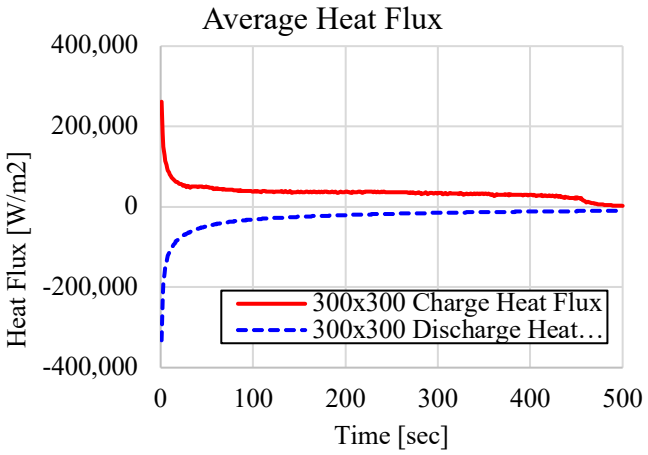

FIGURE 18. Average heat flux to the ROC salt from all walls.

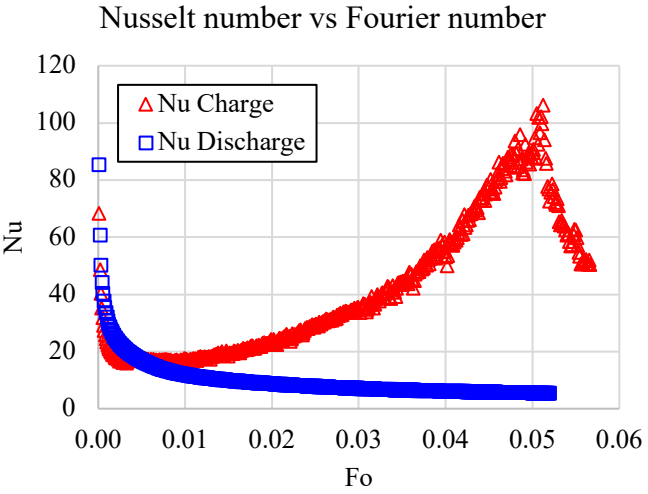

FIGURE 19. Nusselt number variations versus Fourier number representing the ratio of the heat transfer through convection over conduction.

Figure 19 provides a non-dimensional analysis of the results, showing the variations of Nusselt number versus Fourier number during the charge cycle. After the initial decline, Nusselt number increases during the phase change process. The maximum value of Nusselt number (and internal convection coefficient) reaches a maxima at the end of melting. Beyond this point, the heat transfer coefficient and Nusselt number decline. This result provides a tool to estimate the internal connective heat transfer coefficient and charge time.

4. CONCLUSION

A computational model is developed and verified to simulate the heat transfer and phase change process of inorganic ROC salt mixture during charge cycle of an ROC-based thermal energy storage system.

The result shows that the flow and temperature fields during charge and discharge cycles are significantly impacted by phase change process and buoyancy-driven flows. Natural convection is the dominant heat transfer mechanism during charge and discharge cycles and is manifested by boundary layers along the vertical walls of the salt tube and Rayleigh-Bernard instability on the horizontal top and bottom walls.

Dimensionless analysis of the results show that Nusselt number associated with charge process inside the ROC salt tubes changes in the range of 25-90 during the charge cycle with the maximum happening at the end of phase change process.

ACKNOWLEDGEMENTS

This study is supported by the Bureau of Reclamation of the U.S. Department of the Interior by agreement numbers R18AC00087 and R19AC00090, Chino Basin Desalter Authority, and Eastern Municipal Water District. The authors would like to thank ANSYS Inc. for providing COVID licenses.

REFERENCES

[1] Zhang, P, Ma, F, and Xiao, X. "Thermal Energy Storage and Retrieval Characteristics of a Molten-salt Latent Heat Thermal Energy Storage System." *Applied Energy* 173 (2016): 255-71. Web.

[2] Kearney, D, B Kelly, R Cable, N Potrovitza, U Herrmann, P Nava, R Mahoney, J Pacheco, D Blake, and H Price. “Overview on Use of a Molten Salt HTF in a Trough Solar Field.” *NREL TES Workshop-Golden*_Feb03 NREL/PR-550-40028 (February 20, 2003). https://www.nrel.gov/docs/fy03osti/40028.pdf.

[3] Palomar, P., & J., I. (2011). Impacts of Brine Discharge on the Marine Environment. Modelling as a Predictive Tool. *Desalination, Trends and Technologies*. doi:10.5772/14880

[4] Gouda, Venice & Banat, Ibrahim & Riad, W. & Mansour, S.. (1993). Microbiologically Induced Corrosion of UNS N04400 in Seawater. *Corrosion*. 49. 63-73. 10.5006/1.3316036.

[5] *ANSYS Fluent Theory Guide* (16.1 ed.). (2015). ANSYS, Inc.

[6] Arkar, C., & Medved, S. (2005). Influence of accuracy of thermal property data of a phase change material on the result of a numerical model of a packed bed latent heat storage with spheres. *Thermochimica Acta*, 438(1-2), 192-201. https://doi.org/10.1016/j.tca.2005.08.032

[7] Felix Regin, A., Solanki, S., & Saini, J. (2009). An analysis of a packed bed latent heat thermal energy storage system using PCM capsules: Numerical investigation. *Renewable Energy*, 34(7), 1765-1773. https://doi.org/10.1016/j.renene.2008.12.012

[8] V. R. Voller, A. D. Brent, and K. J. Reid. "A Computational Modeling Framework for the Analysis of Metallurgical Solidification Process and Phenomena". Technical report. *Conference for Solidification Processing* Ranmoor House, Sheffield, England. September 1987.

[9] V. R. Voller and C. Prakash. "A Fixed-Grid Numerical Modeling Methodology for Convection-Diffusion Mushy Region Phase-Change Problems". *Int. J. Heat Mass Transfer*. 30. 1709–1720. 1987.

[10] V. R. Voller and C. R. Swaminathan. "Generalized Source-Based Method for Solidification Phase Change". *Numer. Heat Transfer* B,. 19(2). 175–189. 1991.

[11] Bellan, Selvan, Gonzalez-Aguilar, Jose, Romero, Manuel, Rahman, Muhammad M, Goswami, D. Yogi, and Stefanakos, Elias K. "Numerical Investigation of PCM-based Thermal Energy Storage System." *Energy Procedia* 69 (2015): 758-68. Web.

[12] Bellan, S., Gonzalez-Aguilar, J., Romero, M., Rahman, M. M., Goswami, D. Y., Stefanakos, E. K., & Couling, D. (2014). Numerical analysis of charging and discharging performance of a thermal energy storage system with encapsulated phase change material. *Applied Thermal Engineering*, 71(1), 481-500. doi:10.1016/j.applthermaleng.2014.07.009

[13] Bellan, S., Alam, T. E., González-Aguilar, J., Romero, M., Rahman, M. M., Goswami, D., & Stefanakos, E. K. (2015). Numerical and experimental studies on heat transfer characteristics of thermal energy storage system packed with molten salt PCM capsules. *Applied Thermal Engineering*, 90, 970-979. doi:10.1016/j.applthermaleng.2015.07.056

[14] Fornarelli, F., Camporeale, S., Fortunato, B., Torresi, M., Oresta, P., Magliocchetti, L., . . . Santo, G. (2016). CFD analysis of melting process in a shell-and-tube latent heat storage for concentrated solar power plants. *Applied Energy*, 164, 711-722. doi:10.1016/j.apenergy.2015.11.106

[15] Campana, C., Cioccolanti, L., Renzi, M., & Caresana, F. (2019). Experimental analysis of a small-scale scroll expander for low-temperature waste heat recovery in Organic Rankine cycle. Energy, 187, 115929. doi:10.1016/j.energy.2019.115929